Planetary system and star formation science with non-redundant masking on JWST

Anand Sivaramakrishnan[a], David Lafrenière[b], Peter G. Tuthill[c], Michael J. Ireland[c], James P. Lloyd[d], Frantz Martinache[e], Russell B. Makidon[f], Rémi Soummer[f], René Doyon[b], Mathilde Beaulieu[b], Sébastien Parmentier[g] and Charles A. Beichman[h]

[a] Department of Astrophysics, American Museum of Natural History, 79th Street at CPW, New York, NY 10024 United States
[b] Département de Physique, Université de Montréal, Montréal, Qc, H3C 3J7, Canada
[c] School of Physics, University of Sydney, NSW Australia
[d] 230 Space Sciences Building, Cornell University, Ithaca, NY 14853 United States
[e] Subaru Telescope, 650 N. A'ohoku Place, Hilo, HI 96720, United States
[f] Space Telescope Science Institute, 3700 San Martin Drive, Baltimore, MD 21218, United States;
[h] Department of Physics and Astronomy, Stony Brook University, Stony Brook NY 11794 United States
[h] NASA ExoPlanet Science Institute, California Institute of Technology, 1201 California Blvd., Pasadena CA 91125, United States

ABSTRACT

Non-redundant masking (NRM) is a high contrast high resolution technique that is relevant for future space missions dedicated to either general astrophysics or extrasolar planetary astronomy. On the ground NRM has opened a rich target space between 0.5 to 4 resolution elements from bright stars. It enabled moderate contrast very high angular resolution observations that have provided dynamical masses for targets beyond the resolution of the Hubble Space Telescope. Such observations challenge the best models of ultra-cool dwarf stars' atmospheres and interiors. The technique succeeds because it sidesteps the effects of speckle noise that plagues direct imaging at moderate Strehl ratios. On a space telescope NRM mitigates instrument-induced speckle noise, thus enabling high contrast even when images are barely diffraction-limited. The non-redundant mask in the Fine Guidance Sensor Tunable Filter Imager (FGS-TFI) on the James Webb Space Telescope (JWST) will open up a search space between 50 and 400 mas at wavelengths longer than 3.8μm. We present simulations that estimate achievable contrast on JWST, and report preliminary results of a testbed experiment using a mask with the same geometry as JWST's. We expect contrast of the order of 10^4 will be achievable in a 10 ks exposure of an $M = 7$ star, with observing, target acquisition, and data calibration methods common to the three other imaging instruments on board JWST. As an example of the potential science possible with NRM, we show that if a planet were responsible for clearing the inner 5 AU of the disk around HR8799, it would likely be detectable using JWST FGS-TFI's NRM at 4.6 microns. Stars as bright as $M = 3$ will also be observable with JWST's NRM, meshing well with next-generation ground-based extreme adaptive optics coronagraphs. JWST NRM's parameter space is inaccessible to both JWST coronagraphs and future 30-m class ground-based telescopes, especially in the mid-IR.

Keywords: Extrasolar planets, JWST, high contrast imaging, high resolution imaging interferometry

Further author information: (Send correspondence to A.S. E-mail: anand@amnh.org

Space Telescopes and Instrumentation 2010: Optical, Infrared, and Millimeter Wave, edited by Jacobus M. Oschmann Jr., Mark C. Clampin, Howard A. MacEwen, Proc. of SPIE Vol. 7731, 77313W · © 2010 SPIE · CCC code: 0277-786X/10/$18 · doi: 10.1117/12.858161

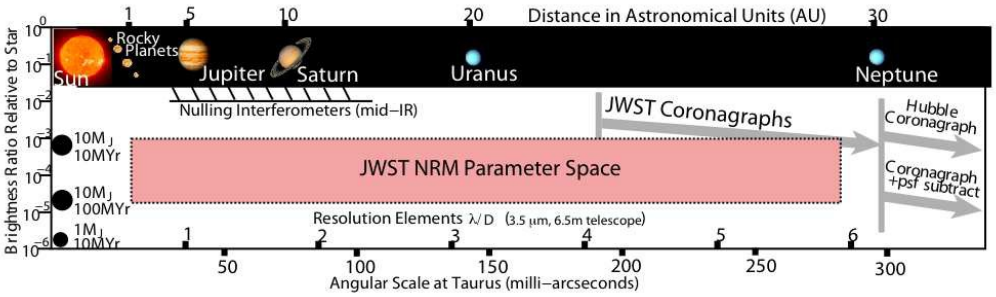

Figure 1. The parameter space available to the newly-added non-redundant sparse aperture mask on JWST's FGS-TFI instrument. It is designed to operate at 3.8 microns and longer. The distance scale at the top marked with solar system planets is shown as an angular scale at the distance of Taurus.

1. INTRODUCTION

Landmark discoveries such as dusty disks imaged around young stellar objects, mass-loss shells of evolved stars and the fascinating time-varying spiral plumes surrounding dusty Wolf-Rayet systems have been reported amongst the increasing number of peer-reviewed papers describing results produced by non-redundant masking (NRM) interferometry[1–15]). However, from the ground the atmosphere limits its performance, as short scale time variability inherent in adaptive optics-corrected point-spread functions (PSFs) makes calibration of NRM (using point sources) difficult.

We present detailed simulations of NRM performance on the James Webb Space Telescope (JWST) to investigate some the exciting planetary science enabled by the NRM on JWST. On JWST NRM will widen the telescope's science reach to include a unique combination of wavelength and angular resolution regimes inaccessible from the ground, even with the advent of extreme adaptive optics (ExAO) and coronagraphs behind 30 m extremely large telescopes of the future. For example, NRM used at 4μm will place warm extrasolar jovians within 4 to 30 AU of F, G, and K dwarfs 30pc from the Sun within JWST's purview (Figure 1).

As it does on ground-based 8-10m class telescopes, NRM adds high resolution capability to large filled-aperture space telescopes without sacrificing their wide utility for general astrophysical observations. Furthermore, the NRM search space is complementary to future coronagraphic space missions dedicated to extrasolar planet imaging and characterization, as well as to ground-based ExAO instruments,[16,17] in that it yields moderate contrasts between 0.5 and $4\lambda/D$ (λ being the observing wavelength, D the telescope diameter). Diffraction-limited stellar coronagraphy, on the other hand, typically covers a search space at higher contrast, at separations larger than $\sim 4\lambda/D$.[18] Even the most aggressive recent coronagraph designs[19,20] cannot search for faint structure or companions closer than about 1.5 angular resolution elements from a star. Post-detection techniques such as Angular or Spectral Differential Imaging[21,22] do not work well at these small angular separations, and spacecraft roll capability on JWST is limited. In addition, any spacecraft manoeuvres use valuable propellant, thereby shortening mission lifetime. This makes NRM an efficient addition to any space telescope that includes general high contrast high angular resolution science on its palette.

We examine the science yield of NRM on JWST's Fine Guidance Sensor's Tunable Filter Imager (FGS-TFI),[23] between 3.8μm and 5μm, operating at a spectral resolution of 100. We simulate a survey of A stars and young stars out to a distance of 140 pc, with approximately hour-long exposures, to show where NRM is useful in survey mode on JWST.

We also simulate observations of HR8799, which posseses three detected giant planetary companions,[24] and a warm disk extending between 5 and 15 AU from the primary.[25] We show that FGS-TFI's NRM could detect a planet 8 magnitudes fainter than HR8799a at 5 AU from the planet. This is an exciting prospect, since the inner edge of the disk might be caused by an unseen planet at that separation from the primary star. Our results can be scaled with both wavelength and optical path difference stability when planning NRM on future missions.

JWST's target acquisition methods being developed for its Mid-Infrared Imager (MIRI), the telescope's pointing stability, and its data calibration pipeline processing will suffice for the high dynamic range NRM

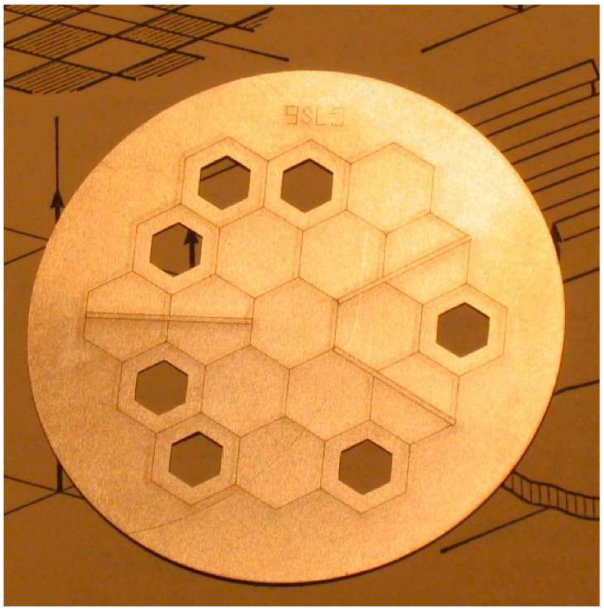

Figure 2. A prototype of the FGS-TFI 7-hole non-redundant pupil mask (holes) overlaid on the JWST primary mirror. The secondary mirror supports are shown engraved on the surface of the part. The mask has undersized holes compared to the segment size to mitigate against up to a 3.8% pupil shear. The projection of the JWST pupil is nominally circumscribed by a circle 39mm in diameter. The part diameter is 50mm

observations we describe here. NRM relies on long-term *stability* of the telescope's wavefront during an exposure that could be up to an hour long, or over a visit of the order of a day, rather than on any stringent requirements on wavefront *quality*. It therefore mitigates some of the risk associated with the complex mechanisms and sequences involved in co-phasing JWST's 18-segment, deployable 6.5 m primary mirror (PM) as the telescope orbits the second Earth-Sun Lagrangian equilibrium point.

2. NRM INTERFEROMETRY AND ITS LIMITS

Interferometry with non-redundant baselines was developed for radio astronomy,[26] and subsequently adapted to optical wavelengths.[27] Today it is used in IR and optical bandpasses, behind instruments not originally developed for sparse aperture interferometry.[1]

Refs. 4, 28–30 and references therein present a fuller description of NRM. In brief, a non-redundant array of subapertures is achieved with N-holes ($\{h_1, h_2, ..., h_N\}$) placed so no vector (baseline) between the centers of two holes is repeated in the pupil plane mask (see Figure 2). The resulting PSF is created by several coherent fringe patterns (each with different angular periods on the detector, thanks to non-redundancy) overlaid across one another. A fringe formed by holes h_i and h_j is quantified by a complex visibility, which has an amplitude (degree of modulation) and a phase (the offset of the fringe's center from the centroid of the PSF). The fringe visibility is the complex product of a Fourier component of the object and a system visibility. When observing a point-source, this phase ϕ_{ij} measures the piston wavefront error between the two holes. A *closure phase* is formed by the addition of three fringe phases created by a triangle of holes, $\{h_i, h_j, h_k\}$, notably $\phi_{ij} + \phi_{jk} + \phi_{ki}$. Although piston wavefront errors change the fringe phases, the closure phases are insensitive to these wavefront errors and only measure source structure. There are $N(N-1)/2$ complex visibilities measurable in the image, $N(N-1)(N-2)/6$ closure phases (or triangles between three apertures), although not all of them are independent. Of these triangles there are $(N-1)(N-2)/2$ independent ones.

On the ground NRM filters out aberrations that pass through an AO system. It is insensitive to the non-common path (NCP) aberrations between the science and sensing arms of the instrument. The NCP issue has only recently been addressed by specialized calibration systems in future ExAO coronagraphic systems utilizing full-aperture pupils.[31] Today's ground-based NRM routinely achieves stability of 0.5 degrees on the closure

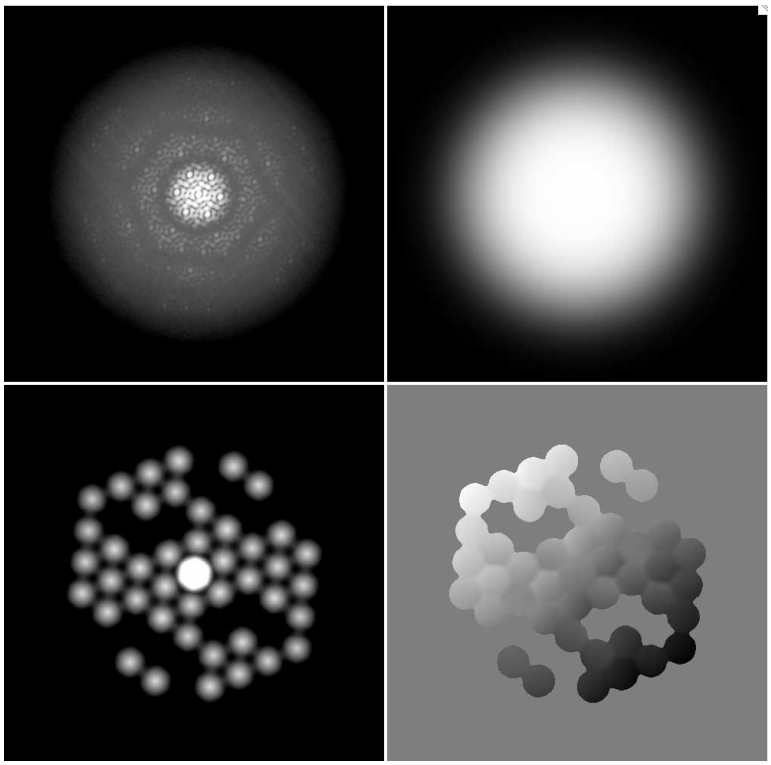

Figure 3. *Top left:* An image of a laser-illuminated pinhole point source shown on a square root stretch after multiplication by an isolating numerical window (*top right*). This PSF is also known as an interferogram. The mask geometry used on the testbed is that of the FGS-TFI mask. The pixel scale on this testbed image is much finer than that of FGS-TFI. *Lower left:* the power spectrum of the windowed PSF shown above it (on a square root scale), showing fringe power on the 21 baselines passed by the mask. *Lower right:* The phase of the Fourier transform of the PSF. The bottom two images comprise the complex visibility of the interferogram. None of the phases wrap, so the phase array is smooth as long as the PSF is well-centered before the analysis. A hundred 20 second exposures, median stacked, yield closure phases of the order of half a degree. The testbed data is amenable to a wider windowing function than typical ground-based data. Since seeing is not an issue here, the testbed provides more space-like conditions than ground-based large telescopes with adaptive optics.

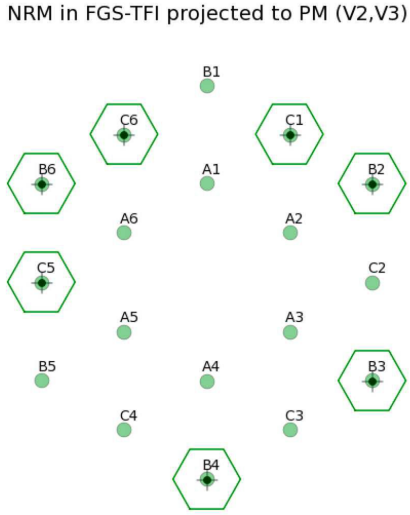

Figure 4. The pupil plane in FGS-TFI is decentered, demagnified, stretched slightly in one dimension, and slightly rotated relative to JWST's primary mirror (PM). The NRM in the JWST FGS-TFI pupil wheel is shown in PM coordinates, after being projected back to the PM using JWST's optical design. Each of the 18 segment centers are indicated with light green circles labelled with their segment names (A1,A2,..., C6). The conceptual design NRM with holes placed in a regular hexagonal grid in (V2,V3) space is shown by small black solid circles at the nominal segment centers' locations (*i.e.,* assuming segments form a regular hexagonal grid in (V2,V3) space). The projected mask's holes in PM space are the 7 green hexagons. Slight misalignments of the holes with their respective PM segment centers will not affect the scientific capabilities of the NRM. However it is preferable that the NRM's holes do not span a segment-to-segment discontinuity. Undersizing of the mask's holes relative to the segments themselves allows for pupil shear up to 3.8% of the pupil diameter before the mask's holes cross segment boundaries.

phase, hence passively stabilizing the phase at the level of $\lambda/500$ to $\lambda/1000$. Early data from our visible light testbed demonstrates closure phases of this order on single images with relatively unsophisticated data analysis. In addition, its data displays very consistent fringe visibilities. The testbed will therefore provide test data for space-like NRM PSFs.

For a point source any closure phase must be zero. A measured non-zero closure phase in the data provides spatial information on the object. A consistent, systematic, instrument-induced departure from a zero closure phase can be measured using a calibration star, and subtracted from a target's closure phase. Conceptually, closure phase data analysis is a model fit of the intensity distribution on sky, the observations being closure phases from all the closed triangles that can be constructed with the given set of baselines. Fringe visibility data makes solving for the actual image (or its measured Fourier components) possible. The inner working angle (IWA) of such an image is $0.5\lambda/D$, the outer working angle (OWA) is set by the shortest non-redundant baseline available. Recovering the measured Fourier components of source structure with NRM imaging using both closure phases and fringe visibilities is a well-posed problem. This is not the case with full aperture imaging. Ground-based fringe visibilities suffer from temporal instabilities due to atmospheric scintillation and transparency variations, though closure phases still extremely useful. On JWST fringe visibilities should be stable since segment reflectivity is unlikely to vary perceptibly during a single exposures, or between science and calibrator exposures.

In practice the dynamic range of space-based NRM may be limited by effects such as a non-isotropic guiding error, imperfect detector flat field knowledge, cosmic rays, intrapixel sensitivity, defective pixels, and pupil wander. Target placement repeatable to a fraction of a pixel on JWST's HAWAII-2RG detectors will ease data calibration difficulties, given the spatial frequency of the detector' flat field structure. Without AO, ground-based NRM, like speckle interferometry, must freeze temporally-varying fringe patterns. AO stabilizes relative piston

	DX/pixel	DY/pixel	Sep./pixel	PA/degrees	Flux ratio
Input	-1.54545	1.27273	2.00206	50.527	6.3e-4
Fit (CP)	-1.58322	1.21041	1.9929	52.601	7.1e-4
Fit (CP) σ	0.18	0.14	0.21	3.1	8.7e-5
Fit (CP+SqV)	-1.62380	1.25609	2.0529	52.276	6.6e-4
Fit (CP+SqV) σ	0.09	0.07	0.09	2.02	3.6e-05

Table 1. Model fits of separation and contrast for a simulated companion 8 magnitudes fainter than the primary star HR8799a using closure phases (CP) only, and squared visibilities as well (CP+SqV). Such a companion could explain the inner edge of the 5-15 AU warm debris disk around HR8799a. The advantage of stable fringe visibilities is apparent from the improved binary parameter fit, and its concomitant reduced uncertainties.

differences between subapertures in the aperture mask. This enables longer exposure times, limited by pixel well-depth, thermal background rates or instrument stability. Once deployed, JWST's primary mirror segments' relative positions (with respect to each other) are expected to drift very slowly. Exposure times will likely be limited by cosmic rays, with a maximum single exposure time measured in hours. Under such conditions NRM opens up a search space completely beyond the reach of ground-based telescopes. Thermal background and atmospheric opacity also limit ground-based imaging longward of about 2μm. JWST's unusual primary mirror geometry and articulation are unlikely to cause problems for NRM interferometry.

For a 0.5m^2 subaperture at 4μm, a 1% filter bandwidth and 50% net quantum efficiency, our preliminary calculations[32] suggested that, given photon noise limitations, $M \simeq 7$ is the faintest target for 10^4 contrast to be achievable in a 10ks exposure, and $M = 12$ is the limit for 10^3 contrast in 10ks. In FGS-TFI, 256×256 sub-array readout capability will enable observations of objects as bright as $M \simeq 3$.

3. A SIMULATED OBSERVATION OF HR8799

HR8799 was found to possess three Jovian mass companions, using ground-based adaptive optics.[24] Recent work[25] show evidence for a warm (150K) disk spanning the range of 5-15 AU from the star, well within the innermost detected planet's orbit. The absence of warm dust within 5 AU of the primary could possibly be explained by the clearing action of an unseen planet orbiting at ~ 5 AU from the primary.[25] Such a companion, if several Jupiters in mass, would be detected by JWST using NRM on FGS-TFI.

An observation sequence of the star HR 8799 was simulated for a wavelength of 4.5 μm. A fake planet 8 magnitudes fainter than HR8799a ($\sim$10 M_{Jup}) was added at an angular separation of $0.13''$($\sim$5 AU); such a hypothetical planet would orbit just inside the innermost dust belt of this system. An individual integration time of 2.64 s was selected to ensure that the peak pixel is well below detector saturation given the star's brightness (1.5 Jy at 4.5 μm). An overall sequence of 100 exposures at each of 9 dither positions was simulated, representing a total integration time of 40 minutes and an elapsed time of roughly 90 minutes.

The simulated images were constructed from a polychromatic TFI NRM PSF oversampled by a factor of 11 relative to the TFI pixel scale of 65 mas.[33] The simulations included a random pointing error of 15 mas rms per axis following each dither and a jitter pointing error of 5 mas rms per axis during each individual exposure. Intrapixel response was also simulated by a Gaussian function assuming on average a pixel corner response of 0.8 with 0.1 rms. After applying the shift and intra-pixel response, the simulated images were binned to the actual TFI pixel scale. Then a flat field error of 0.1% rms was included, as well as read noise, dark current, background signal and photon noise. No bad pixels or cosmic rays were simulated. This numerical scheme was repeated, but without the simulated planet, to generate observations of a calibrator star. Finally, the overall simulation of both the target and calibrator was repeated 11 times and the dispersion of the results over the different trials was used to estimate the uncertainties and detection limits. Our results are presented in Table 1 and Figures 5 and 6.

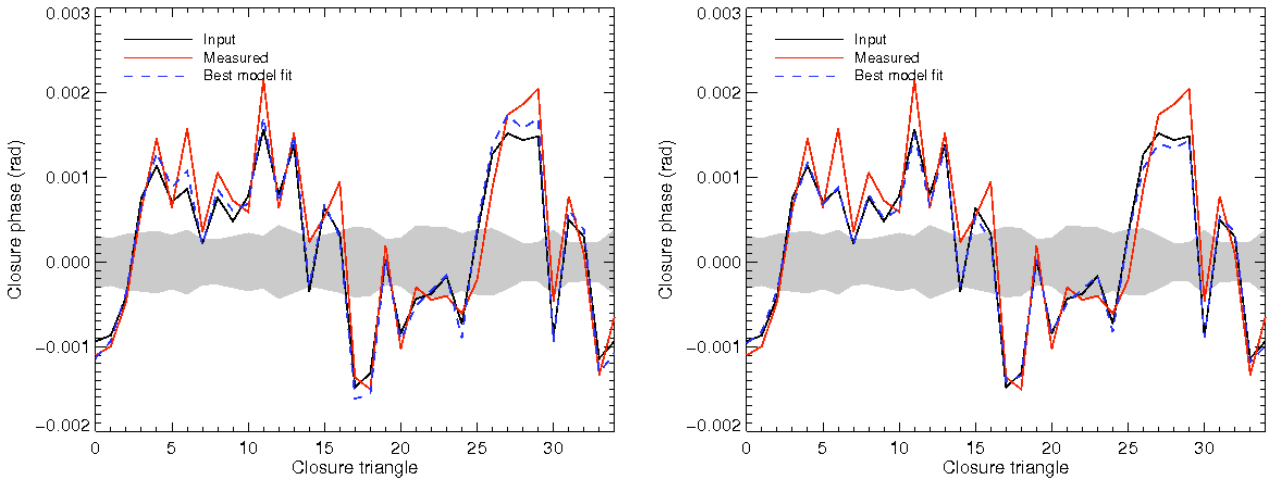

Figure 5. Closure phase values from simulated data using the NRM on JWST-TFI, along with binary model parameter fit values of closure phases. The model consists of a contrast ratio, and the two-dimensional apparent separation of the stars on sky. The simulated target is HR8799a and a hypothesized fourth companion 8 magnitudes fainter than the primary. The existence of this companion might explain the clearing of the warm (150K) inner disk around HR8799a. Uncertainties (standard deviations) in the measured closure phases are shown as the grey area around the expected closure phase value zero. Closure phases and fringe amplitudes calculated from the fake companion model are labelled 'Input'. Simulations include flat field errors, intrapixel sensitivity, guiding errors, target placement errors, read noise, dark current, and photon noise, but no cosmic rays or bad pixels. The best fit models extracted from the simulated data are also shown. *Left:* Binary model fit to only the measured closure phases in the simulated data. *Left:* Binary model fit to both simulated closure phase as well as the fringe visibilities.

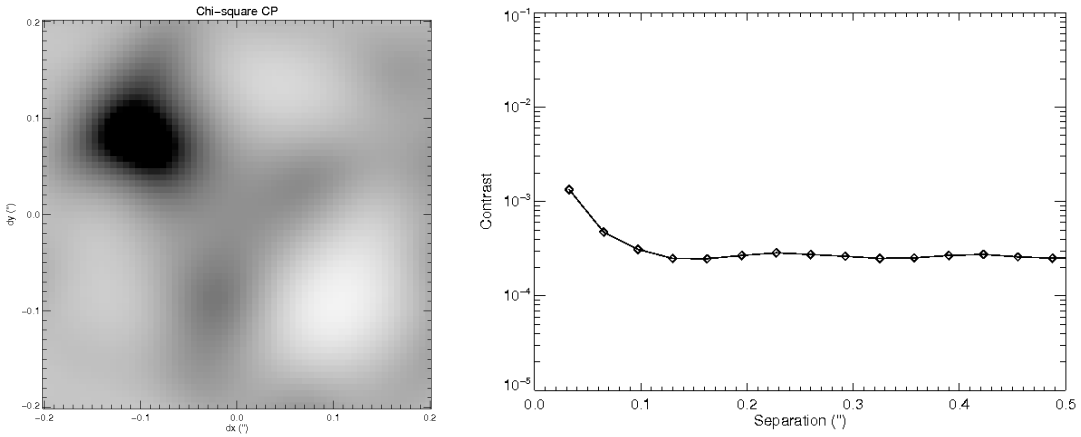

Figure 6. *Left:* The chi-squared plot for the binary model parameters of the hypothesized companion's separation. *Right:* The contrast produced by the detector noise model used in the simulation of the suggested HR8799e companion. A grid of contrasts and positions was run, the contrast is estimated from the scatter of closure phase and fringe amplitude data.

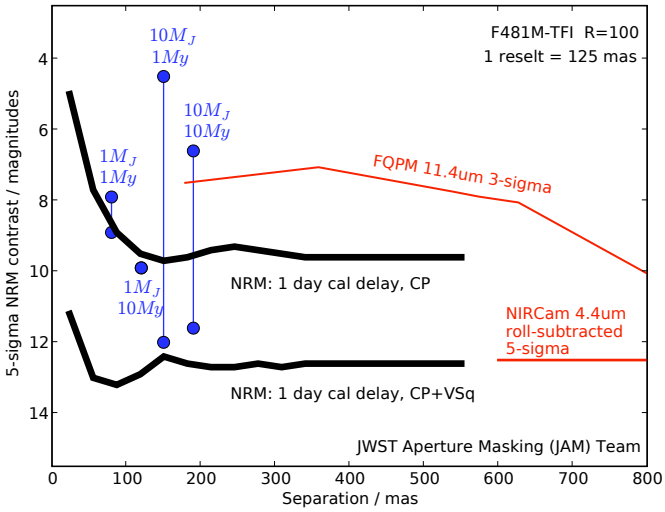

Figure 7. Predicted JWST NRM and coronagraph performance. Dynamic range using only closure phase (CP) as well as closure phase in combination with fringe visibility (CP+VSq) data for 1% bandpass NRM imaging at 4.81μm (using the 7-hole mask shown in Figure 1) in JWST's FGS Tunable Filter Imager (TFI) is plotted (heavy curves). A 1 day delay between the NRM target and calibrator stars, with worst-case attitude-dependent thermally induced primary mirror configuration changes (breathing), guiding errors, and measured detector intra-pixel sensitivity are simulated. In a 10 ks exposure on an $M = 7$ target, photon noise sets a 10 magnitude dynamic range limit. 10% bandwidths will produce similar results in 1ks. The range of estimated contrasts between a solar type star and 1 and 10 Jupiter mass planets, at ages of 1 and 10 Myr (Ref. 34, 35) are shown (vertical blue lines placed at arbitrary separations). This mask will enable JWST to detect protoplanets in Taurus. The same mask in JWST NIRCam will produce 1 to 2 magnitudes less contrast at 2 μm, at half the corresponding angular separation. NRM performance at 4.8 μm drops outside about 600mas. NIRCam's linear band-limited coronagraph performance using planned JWST roll angles[36] complements the FGS-TFI NRM search space. The JWST MIRI four quadrant phase mask coronagraph 11 μm contrast curve,[37] assuming a static 5mas pointing error between target and calibrator, no guiding error, unrestricted telescope roll capability, and no error in calibration star placement is also plotted. Jovian planets are brighter at this wavelength than at 3-5 μm.

4. THE EFFECT OF MIRROR SEGMENT DRIFT ON NRM CONTRAST

We used ten Monte Carlo realizations of JWST's exit pupil wavefront that conform to JWST's wavefront error budget.[39] These OPDs,[40] provided with the JWPSF[41] software distribution, represent the wavefront in JWST NIRCam's short-wavelength channel. They assume particular low-, mid-, and high-spatial frequency wavefront error allocations to JWST's Optical Telescope Element (OTE) and Integrated Science Instrument Module (ISIM). These realizations yield PSFs at 2μm with Strehl ratios above 80%. They are estimates, given the expected residual wavefront error 14 days after active tuning of the JWST primary mirror (PM) figure has been performed, and the telescope slewed from a spacecraft attitude with the most thermal load from the Sun to one with the least such thermal load. To preserve the individual segment wavefront errors associated with one realization of the 18 segments in JWST's PM, we extracted the individual segment piston errors from each of the ten wavefront maps, and used them to create ten instances of a single thermally perturbed set of PM segments.

Using methods described in Refs. 42–45, we simulated images on a 9-fold finer grid than the 65 mas FGS-TFI detector pixel pitch. We dithered the oversampled PSFs by one sample spacing to model pointing errors of 7mas per axis. Intra-pixel quantum efficiency was modeled as a quadratic, ranging from unity at a pixel center to 0.8 at a pixel corner. We then binned the 9×9 dithered subsampled PSFs to create an image on the FGS-TFI pixel scale. We did not explicitly simulate photon noise, read out noise ($\sim 15e^-$ rms for a double-correlated sample), or detector flat field errors, although our detection threshold calculations have taken some experience-based account of these processes.

Simulated data were analyzed with a pipeline used for Keck, Palomar, and VLT data. (*e.g.,* Ref. 46). Nine

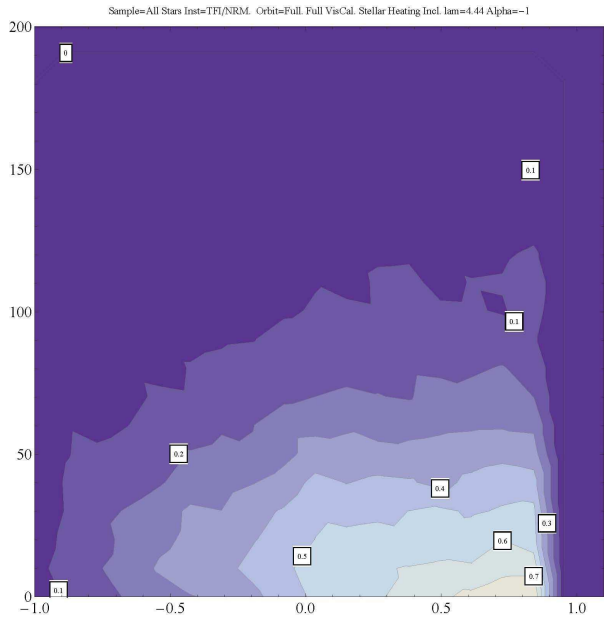

Figure 8. NRM detection probabilities for FGS-TFI at 4.44 μm, drawing from a large sample of young nearby stars. Companion mass is cut off above 10 Jupiter masses. Contours show the estimated probability of finding a planet with a given mass (in Jupiter masses, log scale), on the horizontal axis, and a given semi-major axis (AU, vertical axis) within nominal performance (a 10 magnitude contrast floor imposed on the curves in Fig. 7). The exposure time assumed is about 1 hour per source. Better detection probabilities would result from longer exposures on an individual object. After Beichman et al. 2010.[38]

of the ten PSF realizations in a set were taken to be calibrator observations, and one of the ten was taken to be the target observation. This process was repeated for several choices of target PSF. Rather than replicating the complex Monte-Carlo process of Ref. 46, we chose to use a simple detection threshold of 5σ, with closure-phase and visibility standard deviations calculated from scatter within the 9 calibrator observations. Note that typical 99.9% detection thresholds in Ref. 46 were $\sim$4 to 4.5σ with a more complete Monte-Carlo, which was verified by the lack of numerous false detections in that paper. We therefore believe our 5σ limit is conservative.

Figure 7 shows the contrast achieved with dynamic range calculated two ways: first, using only the closure phases (labelled CLP) for a comparison with current ground-based results, and second, using both closure phases and fringe visibilities (labelled CLP+VIS), to estimate the full range of contrast available to JWST. Contrast between M_J and $10M_J$ planets 1 and 10 Myr old and a parent G2V dwarf are shown in the figure. We find our mask designs produce these estimated contrasts even when the detector's pixel pitch is slightly worse than Nyquist. The very highest contrast shown is obtained using both closure phases as well as fringe visibilities.

5. WAVEFRONT SENSING AND CONTROL RISK MITIGATION WITH NRM

NRM brings both scientific and operational advantages to JWST, given the telescope's segmented architecture and planned co-phasing methods during commissioning.[47–49] JWST NIRCAM is the primary wavefront sensor for JWST. The original baseline operational scheme is to use NIRCam for all JWST's wavefront sensing. The presence of the non-redundant mask in FGS-TFI provides an independent measure of the wavefront. By stepping the wheel holding the NRM through the pupil, the relative piston between 11 of JWST's 18 segments can be measured to interferometric accuracy. With the 1% bandwidth of FGS-TFI the capture range of this process is of the order of 250μm. when used at the longest wavelength available to FGS-TFI. Given that wavefront sensing and control is one of JWST's biggest risks, NRM in FGS-TFI provides significant risk mitigation.

Camera-specific wavefront knowledge can feed into data reduction, benefiting science that requires thorough understanding of temporal, spatial, and chromatic variations in the PSF. In addition, NRM observations determine stellar multiplicity at the highest resolution and contrast possible. Such observations can eliminate

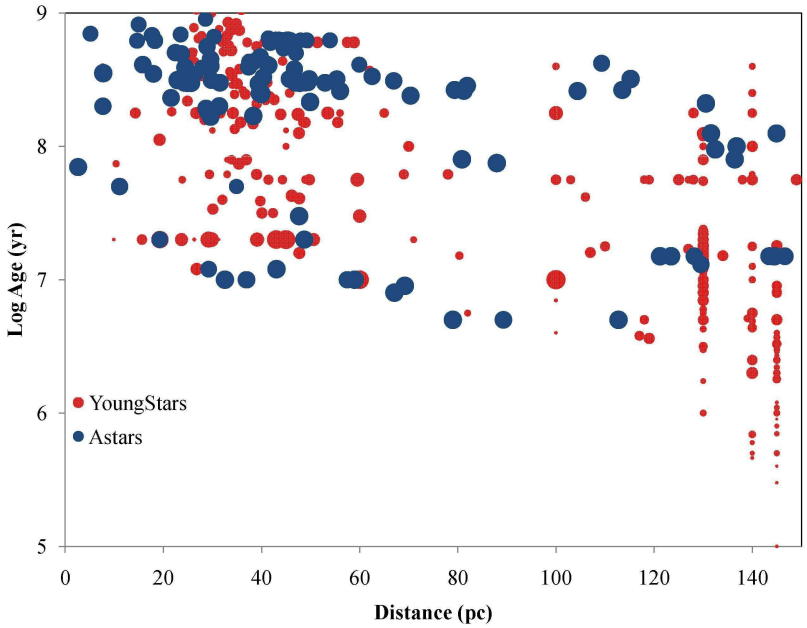

Figure 9. Distribution of stellar ages with distance in the sample used to generate the detection probability shown in Fig. 8. The sample comprises stars younger than 5Myr and closer than 140pc from the Sun, and stars older than 10Myr that are within 50pc of the Sun. After Beichman et al. 2010.[38]

inappropriate wavefront sensing or guide star choices. Images taken as the mask is stepped across the pupil (or vice versa) will measure pupil location without specialized pupil imaging optics. Such information is relevant for IR instrument and telescope maintenance.

6. CONCLUSION

Detailed simulations with detector effects such as intrapixel sensitivity, telescope pointing errors, flat field inaccuracies, inexact target placement on the detector, read noise, dark current, photon noise, time-varying mirror figure errors, and existing data reduction methods demonstrate that a non-redundant aperture mask on the Tunable Filter Imager on board JWST enables some exciting high resolution high contrast imaging. The 7-hole mask in the Fine Guidance Sensor's Tunable Filter Imager will image protoplanets in Taurus, and could detect a hypothesised planet responsible for sculpting the inner edge of the warm disk found at 5 AU from HR8799. Aperture masking also provides JWST with alternative, risk-reducing wavefront measuring techniques, while increasing the science output of JWST substantially, paving the way for future missions with NRM instrumentation. Future missions can increase the science payoff with more optimized NRM modes, making the technique even more relevant for galactic, extragalactic, and cosmological observations.

ACKNOWLEDGMENTS

We thank P. A. Lightsey, J. C. Mather, M. Robberto and N. Rowlands for encouraging discussions and helpful information. This work is supported in part by the National Science Foundation under Grant AST 08-04417, NASA grant APRA08-0117, and JPL grant No. RSA 1330128.

REFERENCES

[1] Tuthill, P. G., Monnier, J. D., Danchi, W. C., and Haniff, C. A., "Michelson interferometry with Keck I," in [*SPIE Conference Series*], Reasenberg, R. D., ed., **3350**, 839–846 (July 1998).

[2] Monnier, J. D., Tuthill, P. G., and Danchi, W. C., "Pinwheel Nebula around WR 98A," *ApJL* **525**, L97–L100 (Nov. 1999).

[3] Monnier, J. D., Tuthill, P. G., Lopez, B., Cruzalebes, P., Danchi, W. C., and Haniff, C. A., "The Last Gasps of VY Canis Majoris: Aperture Synthesis and Adaptive Optics Imagery," *ApJ* **512**, 351–361 (Feb. 1999).

[4] Tuthill, P. G., Monnier, J. D., Danchi, W. C., Wishnow, E. H., and Haniff, C. A., "Michelson Interferometry with the Keck I Telescope," *PASP* **112**, 555–565 (Apr. 2000).

[5] Tuthill, P. G., Monnier, J. D., and Danchi, W. C., "A dusty torus around the luminous young star LkHα101," *Nature* **409**, 1012–1014 (Feb. 2001).

[6] Tuthill, P. G., Monnier, J. D., Danchi, W. C., Hale, D. D. S., and Townes, C. H., "Imaging the Disk around the Luminous Young Star LkHα 101 with Infrared Interferometry," *ApJ* **577**, 826–838 (Oct. 2002).

[7] Tuthill, P. G., Monnier, J. D., and Danchi, W. C., "Multiwavelength Diffraction-limited Imaging of the Evolved Carbon Star IRC +10216. II.," *ApJ* **624**, 352–358 (May 2005).

[8] Tuthill, P., Monnier, J., Tanner, A., Figer, D., Ghez, A., and Danchi, W., "Pinwheels in the Quintuplet Cluster," *Science* **313**, 935–+ (Aug. 2006).

[9] Lloyd, J. P., Martinache, F., Ireland, M. J., Monnier, J. D., Pravdo, S. H., Shaklan, S. B., and Tuthill, P. G., "Direct Detection of the Brown Dwarf GJ 802B with Adaptive Optics Masking Interferometry," *ApJL* **650**, L131–L134 (Oct. 2006).

[10] Pravdo, S. H., Shaklan, S. B., Wiktorowicz, S. J., Kulkarni, S., Lloyd, J. P., Martinache, F., Tuthill, P. G., and Ireland, M. J., "Masses of Astrometrically Discovered and Imaged Binaries: G78-28AB and GJ 231.1BC," *ApJ* **649**, 389–398 (Sept. 2006).

[11] Martinache, F., Lloyd, J. P., Ireland, M. J., Yamada, R. S., and Tuthill, P. G., "Precision Masses of the Low-Mass Binary System GJ 623," *ApJ* **661**, 496–501 (May 2007).

[12] Tuthill, P. G. and Lloyd, J. P., "A Symmetric Bipolar Nebula Around MWC 922," *Science* **316**, 247– (Apr. 2007).

[13] Ireland, M. J. and Kraus, A. L., "The Disk Around CoKu Tauri/4: Circumbinary, Not Transitional," *ApJL* **678**, L59–L62 (May 2008).

[14] Ireland, M. J., Kraus, A., Martinache, F., Lloyd, J. P., and Tuthill, P. G., "Dynamical Mass of GJ 802B: A Brown Dwarf in a Triple System," *ApJ* **678**, 463–471 (May 2008).

[15] Tuthill, P. G., Monnier, J. D., Lawrance, N., Danchi, W. C., Owocki, S. P., and Gayley, K. G., "The Prototype Colliding-Wind Pinwheel WR 104," *ApJ* **675**, 698–710 (Mar. 2008).

[16] Macintosh, B., Graham, J., Palmer, D., Doyon, R., Gavel, D., Larkin, J., Oppenheimer, B., Saddlemyer, L., Wallace, J. K., Bauman, B., Evans, J., Erikson, D., Morzinski, K., Phillion, D., Poyneer, L., Sivaramakrishnan, A., Soummer, R., Thibault, S., and Veran, J.-P., "The Gemini Planet Imager," in [*SPIE Conference Series*], **6272** (July 2006).

[17] Beuzit, J.-L., Feldt, M., Dohlen, K., Mouillet, D., Puget, P., Wildi, F., Abe, L., Antichi, J., Baruffolo, A., Baudoz, P., Boccaletti, A., Carbillet, M., Charton, J., Claudi, R., Downing, M., Fabron, C., Feautrier, P., Fedrigo, E., Fusco, T., Gach, J.-L., Gratton, R., Henning, T., Hubin, N., Joos, F., Kasper, M., Langlois, M., Lenzen, R., Moutou, C., Pavlov, A., Petit, C., Pragt, J., Rabou, P., Rigal, F., Roelfsema, R., Rousset, G., Saisse, M., Schmid, H.-M., Stadler, E., Thalmann, C., Turatto, M., Udry, S., Vakili, F., and Waters, R., "SPHERE: a planet finder instrument for the VLT," in [*Society of Photo-Optical Instrumentation Engineers (SPIE) Conference Series*], *Society of Photo-Optical Instrumentation Engineers (SPIE) Conference Series* **7014** (Aug. 2008).

[18] Sivaramakrishnan, A., Koresko, C. D., Makidon, R. B., Berkefeld, T., and Kuchner, M. J., "Ground-based Coronagraphy with High-order Adaptive Optics," *ApJ* **552**, 397–408 (May 2001).

[19] Mawet, D., Serabyn, E., Liewer, K., Burruss, R., Hickey, J., and Shemo, D., "The Vector Vortex Coronagraph: Laboratory Results and First Light at Palomar Observatory," *ApJ* **709**, 53–57 (Jan. 2010).

[20] Guyon, O., Pluzhnik, E. A., Galicher, R., Martinache, F., Ridgway, S. T., and Woodruff, R. A., "Exoplanet Imaging with a Phase-induced Amplitude Apodization Coronagraph. I. Principle," *ApJ* **622**, 744–758 (Mar. 2005).

[21] Marois, C., Lafrenière, D., Doyon, R., Macintosh, B., and Nadeau, D., "Angular Differential Imaging: A Powerful High-Contrast Imaging Technique," *ApJ* **641**, 556–564 (Apr. 2006).

[22] Lafrenière, D., Doyon, R., Nadeau, D., Artigau, É., Marois, C., and Beaulieu, M., "Improving the Speckle Noise Attenuation of Simultaneous Spectral Differential Imaging with a Focal Plane Holographic Diffuser," *ApJ* **661**, 1208–1217 (June 2007).

[23] Doyon, R., Hutchings, J., Rowlands, N., Beaulieu, M., Lafreniére, D., Abraham, R., Chayer, P., Ferrarese, L., Fullerton, A. W., Jayawardhana, R., Johnston, D., Martel, A., Meyer, M. R., Pipher, J., Sawicki, M., Sivaramakrishnan, A., Volk, K., and Saad, K., "The JWST tunable filter imager (TFI)," in [*Society of Photo-Optical Instrumentation Engineers (SPIE) Conference Series*], *Presented at the Society of Photo-Optical Instrumentation Engineers (SPIE) Conference* **7010** (Aug. 2008).

[24] Marois, C., Macintosh, B., Barman, T., Zuckerman, B., Song, I., Patience, J., Lafrenière, D., and Doyon, R., "Direct Imaging of Multiple Planets Orbiting the Star HR 8799," *Science* **322**, 1348– (Nov. 2008).

[25] Su, K. Y. L., Rieke, G. H., Stapelfeldt, K. R., Malhotra, R., Bryden, G., Smith, P. S., Misselt, K. A., Moro-Martin, A., and Williams, J. P., "The Debris Disk Around HR 8799," *ApJ* **705**, 314–327 (Nov. 2009).

[26] Jennison, R. C., "A phase sensitive interferometer technique for the measurement of the Fourier transforms of spatial brightness distributions of small angular extent," *MNRAS* **118**, 276–+ (1958).

[27] Baldwin, J. E., Haniff, C. A., Mackay, C. D., and Warner, P. J., "Closure phase in high-resolution optical imaging," *Nature* **320**, 595–597 (Apr. 1986).

[28] Haniff, C. A., Buscher, D. F., Christou, J. C., and Ridgway, S. T., "Synthetic aperture imaging at infrared wavelengths," *MNRAS* **241**, 51P–56P (Nov. 1989).

[29] Readhead, A. C. S., Nakajima, T. S., Pearson, T. J., Neugebauer, G., Oke, J. B., and Sargent, W. L. W., "Diffraction-limited imaging with ground-based optical telescopes," *AJ* **95**, 1278–1296 (Apr. 1988).

[30] Monnier, J. D., "Optical interferometry in astronomy," *Reports on Progress in Physics* **66**, 789–857 (May 2003).

[31] Sivaramakrishnan, A., Soummer, R., Pueyo, L., Wallace, J. K., and Shao, M., "Sensing Phase Aberrations behind Lyot Coronagraphs," *ApJ* **688**, 701–708 (Nov. 2008).

[32] Sivaramakrishnan, A., Soummer, R., Carr, G. L., Dorrer, C., Bolognesi, A., Zimmerman, N., Oppenheimer, B. R., Roberts, R., and Greenbaum, A., "Calibrating IR optical densities for the Gemini Planet Imager extreme adaptive optics coronagraph apodizers," in [*Society of Photo-Optical Instrumentation Engineers (SPIE) Conference Series*], *Society of Photo-Optical Instrumentation Engineers (SPIE) Conference Series* **7440** (Aug. 2009).

[33] Soummer, R., Pueyo, L., Sivaramakrishnan, A., and Vanderbei, R. J., "Fast computation of Lyot-style coronagraph propagation," *Optics Express* **15**, 15935–15951 (2007).

[34] Baraffe, I., Chabrier, G., Barman, T. S., Allard, F., and Hauschildt, P. H., "Evolutionary models for cool brown dwarfs and extrasolar giant planets. The case of HD 209458," *Astronomy and Astrophysics* **402**, 701–712 (May 2003).

[35] Marley, M. S., Fortney, J. J., Hubickyj, O., Bodenheimer, P., and Lissauer, J. J., "On the Luminosity of Young Jupiters," *ApJ* **655**, 541–549 (Jan. 2007).

[36] Krist, J. E., Beichman, C. A., Trauger, J. T., Rieke, M. J., Somerstein, S., Green, J. J., Horner, S. D., Stansberry, J. A., Shi, F., Meyer, M. R., Stapelfeldt, K. R., and Roellig, T. L., "Hunting planets and observing disks with the JWST NIRCam coronagraph," in [*SPIE Conference Series*], **6693** (Sept. 2007).

[37] Cavarroc, C., Boccaletti, A., Baudoz, P., Amiaux, J., and Regan, M., "Target Acquisition for MIRI Coronagraphs," *PASP* **120**, 1016–1027 (Sept. 2008).

[38] Beichman, C. A., Krist, J., Trauger, J. T., Greene, T., Oppenheimer, B., Sivaramakrishnan, A., Doyon, R., Boccaletti, A., Barman, T. S., and Rieke, M., "Imaging Young Giant Planets From Ground and Space," *PASP* **122**, 162–200 (Feb. 2010).

[39] Lightsey, P. A., Barto, A. A., and Contreras, J., "Optical performance for the James Webb Space Telescope," in [*SPIE Conference Series*], Mather, J. C., ed., **5487**, 825–832 (Oct. 2004).

[40] Barto, A. A. and Lightsey, P. A., "Optical performance modeling of the James Webb Space Telescope," in [*Optical, Infrared, and Millimeter Space Telescopes.*], Mather, J. C., ed., *Proc. SPIE* **5487**, 867–874 (Oct. 2004).

[41] Cox, C. and Hodge, P., "Point-spread function modeling for the James Webb Space Telescope," in [*Space Telescopes and Instrumentation I: Optical, Infrared, and Millimeter.*], John C. Mather, Howard A. MacEwen, and Mattheus W. M. de Graauw, eds., *Proc. SPIE* **6265**, 62650W (2006).

[42] Sivaramakrishnan, A., Makidon, R. B., Figer, D. F., Jedrzejewski, R. I., Bushouse, H. A., Krist, J. E., Stockman, H. S. P., Hodge, P., Dencheva, N. M., Rauscher, B. J., Laidler, V. G., Ohara, C. M., Redding, D. C., Im, M., and Offenberg, J. D., "NIRCAM image simulations for NGST wavefront sensing," in [*IR Space Telescopes and Instruments.*], John C. Mather, ed., *Proc. SPIE* **4850**, 388–397 (2003).

[43] Sivaramakrishnan, A., Morse, E. C., Makidon, R. B., Bergeron, L. E., Casertano, S., Figer, D. F., Acton, D. S., Atcheson, P. D., and Rieke, M. J., "Limits on routine wavefront sensing with NIRCam on JWST," in [*SPIE Conference Series*], Mather, J. C., ed., **5487**, 909–917 (Oct. 2004).

[44] Soummer, R., Pueyo, L., Sivaramakrishnan, A., and Vanderbei, R. J., "Fast computation of Lyot-style coronagraph propagation," *Optics Express* **15**, 15935–+ (2007).

[45] Makidon, R. B., Sivaramakrishnan, A., Soummer, R., Anderson, J., and van der Marel, R. P., "Towards observing extrasolar giant-planet environments with JWST," in [*SPIE Conference Series*], **7010** (Aug. 2008).

[46] Kraus, A. L., Ireland, M. J., Martinache, F., and Lloyd, J. P., "Mapping the Shores of the Brown Dwarf Desert. I. Upper Scorpius," *ApJ* **679**, 762–782 (May 2008).

[47] Sivaramakrishnan, A., "Coarse Phasing JWST: an Operations Concept Document (JWST-STScI-000378)," STScI, Baltimore (2004).

[48] Sivaramakrishnan, A., Makidon, R. B., Acton, D. S., and Shi, F., "Coarse Phasing JWST using Dispersed Fringe Sensing and Dispersed Hartmann Sensing during Commissioning (JWST-STScI-000341)," STScI, Baltimore (2005).

[49] Long, K. S., "JWST Mission Operations Concept Document (JWST-OPS-002018)," STScI, Baltimore (2006). Revision B.